



Electrochemical properties for high surface area and improved electrical conductivity of platinum-embedded porous carbon nanofibers



Geon-Hyoung An^a, Hyo-Jin Ahn^{a,*}, Woong-Ki Hong^{b,**}

^a Department of Materials Science and Engineering, Seoul National University of Science and Technology, Seoul 139-743, Republic of Korea

^b Jeonju Center, Korea Basic Science Institute, Jeonju, Jeollabuk-do 561-180, Republic of Korea

HIGHLIGHTS

- Porous and non-porous CNFs with and without Pt metal nanoparticles using electrospinning.
- A combined study of the surface area, mesoporous volume, and electrical conductivity of electrode materials.
- Synergistic effects of the high specific surface area with a large mesopore volume, and superior electrical conductivity.

ARTICLE INFO

Article history:

Received 21 July 2014

Received in revised form

23 September 2014

Accepted 14 October 2014

Available online 20 October 2014

Keywords:

Electrochemical capacitors

Carbon nanofibers

High surface area

Pore volume fraction

Electrical conductivity

ABSTRACT

Four different types of carbon nanofibers (CNFs) for electrical double-layer capacitors (EDLCs), porous and non-porous CNFs with and without Pt metal nanoparticles, are synthesized by an electrospinning method and their performance in electrical double-layer capacitors (EDLCs) is characterized. In particular, the Pt-embedded porous CNFs (PCNFs) exhibit a high specific surface area of $670 \text{ m}^2 \text{ g}^{-1}$, a large mesopore volume of 55.7%, and a low electrical resistance of 1.7×10^3 . The synergistic effects of the high specific surface area with a large mesopore volume, and superior electrical conductivity result in an excellent specific capacitance of 130.2 F g^{-1} , a good high-rate performance, superior cycling durability, and high energy density of $16.9\text{--}15.4 \text{ W h kg}^{-1}$ for the performance of EDLCs.

© 2014 Elsevier B.V. All rights reserved.

1. Introduction

Electrochemical capacitors (ECs) have recently attracted the interest of researchers because of their potential application in electronic devices, electric vehicles, large-scale industrial equipment, and memory back-up devices, and their various advantages such as high power densities, fast-charge/discharge rates, excellent cycling efficiencies, and long cycling lifetimes [1–5].

Generally, ECs can be classified into two categories, electrical double-layer capacitors (EDLCs) and pseudo capacitors, based on two distinct energy storage mechanisms. EDLCs can store charge

based on the capacitive (non-Faradaic) process, which harnesses the separation of charge between the electrolyte and electrode interface; in this case, the electrode materials use carbon-based materials such as activated carbon, graphene, carbon nanotubes (CNTs), and carbon nanofibers (CNFs) [6]. Meanwhile, pseudo capacitors are based on a redox process (Faradaic) that entails reversible electron-exchange reactions in the proximity of the electrode surface; in this process, the electrode materials use transition metal oxides (e.g. RuO_2 , MnO_2 , and Co_3O_4) and a redox polymer (e.g. polypyrroles, polyanilines, and polythiophenes) [7]. Compared with EDLCs, pseudo capacitors can achieve higher specific capacitance and relatively higher energy densities due to benefits of the redox process (Faradaic) than EDL capacitance. However, the practical applications of these electro-active materials in pseudo-capacitors remain limited due to their disadvantages of high cost and poor cycling stability [8]. In contrast, EDLCs offer attractive advantages such as low cost, high power densities,

* Corresponding author. Tel.: +82 2 970 6622; fax: +82 2 973 6657.

** Corresponding author. Tel.: +82 63 711 4511; fax: +82 63 270 4308.

E-mail addresses: hjahn@seoultech.ac.kr (H.-J. Ahn), wkh27@kbsi.re.kr (W.-K. Hong).

high rate capabilities, and excellent cycling stabilities, in spite of relatively lower energy densities than pseudo capacitors and conventional rechargeable batteries.

To improve the energy density and capacitance of EDLCs, various carbon based-materials have been investigated and reported as active electrode materials; further, for use in high-performance EDLCs, these materials must meet the requirements of high surface area, high electrical conductivity, superior electrochemical stability, open porosity, among others [9–12]. In particular, among the carbon-based materials, CNFs have recently received increasing attention as active materials due to their lots of advantages such as low cost, large surface areas ($462 \text{ m}^2 \text{ g}^{-1}$), high aspect ratio, low electrical resistance, and chemical stability [13–15]. For example, Kim et al. [16] synthesized porosity-controlled CNF electrodes by an electrospinning method of two immiscible polymer blends (PAN and pitch) followed by thermal treatment in which the porosity-controlled CNFs have a good specific capacitance of 130.7 F g^{-1} at a current density of 1 A g^{-1} and energy density of 15.0 W h kg^{-1} . Chen et al. [17] investigated nitrogen-doped porous carbon nanofibers synthesized by the carbonization of macroscopic-scale carbonaceous nanofibers coated with polypyrrole; in this work, the composite nanofibers exhibited a good specific capacitance of 202.0 F g^{-1} at a current density of 1.0 A g^{-1} , good cycling durability (above 97% of the initial capacitance), and an energy density of 7.11 W h kg^{-1} .

Until now, a combined study of the surface area, mesoporous volume, and electrical conductivity of electrode materials, with similar CNF diameters, has not been reported for EDLCs. Therefore, we synthesized Pt-embedded porous carbon nanofibers (Pt/PCNFs) by an electrospinning method followed by carbonization and investigated their electrochemical capacitor properties such as their specific capacitance, high-rate performance, energy density, and cycling durability. The obtained results demonstrate that the Pt/PCNFs exhibit significant potential as efficient electrode materials for high-performance EDLCs with the improvement of electrochemical performances based on a specific surface area of $670 \text{ m}^2 \text{ g}^{-1}$, a large mesopore volume of 55.7%, and a low electrical resistance of $R_{\text{ave}} = 1.7 \times 10^3$.

2. Experimental

2.1. Chemicals

Polyacrylonitrile (PAN, $M_w = 150,000$), poly(styrene-co-acrylonitrile) (SAN, $M_w = \sim 165,000$), chloroplatinic acid hydrate ($\text{H}_2\text{PtCl}_6 \cdot x\text{H}_2\text{O}$, $\geq 99.9\%$), *N,N*-Dimethylformamide (DMF, 99.8%), and *N*-methyl-2-pyrrolidinone (NMP, 99.5%) were purchased from Sigma–Aldrich. All chemicals were used without further purification.

2.2. Synthesis of CNFs, PCNFs, Pt/CNFs, and Pt/PCNFs

Four different types of samples as electrode materials for EDLCs were synthesized by an electrospinning method followed by carbonization. All four samples identified as CNFs, porous CNFs (PCNFs), Pt-embedded CNFs (Pt/CNFs), and Pt/PCNFs. Electrospinning solutions were prepared by the four different types of solution mixtures. First, CNFs were fabricated using a solution mixture of 10 wt% PAN in DMF. Second, PCNFs were synthesized by dissolving 10 wt% PAN and 0.5 wt% SAN in DMF. Then, Pt/CNFs were prepared using a mixture solution of 10 wt% PAN and 2 wt% $\text{H}_2\text{PtCl}_6 \cdot x\text{H}_2\text{O}$ in DMF. Finally, Pt/PCNFs were synthesized by dissolving 10 wt% PAN, 0.5 wt% SAN and 2 wt% $\text{H}_2\text{PtCl}_6 \cdot x\text{H}_2\text{O}$ in DMF. Electrospinning process was carried out at a voltage of 13 kV and a feed rate of 0.03 mL h^{-1} , with a syringe needle-to-collector distance

of 15 cm, and approximately 10% humidity in the chamber. All the as-spun nanofibers were stabilized by heat treatment at $280 \text{ }^\circ\text{C}$ for 2 h in air, and then they were carbonized at $800 \text{ }^\circ\text{C}$ for 2 h in N_2 gas (99.999%).

2.3. Characterization

The morphologies and structures were examined by field emission-scanning electron microscopy (FESEM, Hitachi S-4800) and transmission electron microscopy (TEM, JEOL 2100F). The crystal structures and chemical bonding states were characterized by X-ray diffractometry (XRD, Rigaku D/MAX2500 V) and X-ray photoelectron spectroscopy (XPS, ESCALAB 250 equipped with an Al K α X-ray source), respectively. Specific surface area, pore volume, average pore diameter, and pore volume fraction measurements were examined by the Brunauer–Emmett–Teller (BET) using N_2 adsorption at 77 K.

2.4. Characterization of electrical conductivity

The electrical conductivities of four different types of CNFs were examined using a semiconductor parameter system (Keithley, 4200-SCS). The homogenized mixture materials of the obtained 80 wt% CNFs, 10 wt% Ketjen black (Mitsubishi Chemical, ECP-600JD) as a conducting material, and 10 wt% poly(vinylidene difluoride) (PVDF, Alfa Aesar) as a binder in NMP were coated on a glass substrate in a film size of $1 \text{ cm} \times 1 \text{ cm}$ and the resultant CNF films were dried in air at $100 \text{ }^\circ\text{C}$ for 12 h. The thickness and mass of all resultant CNF films were fixed at approximately 0.1 mm and 10 mg, respectively. For electrical conductivity measurements of all resultant CNF films, metal electrodes consisting of Al (100 nm)/Au (100 nm) were deposited on CNF films/glass by a thermal evaporator, and respective electrodes were defined as the source and drain electrodes using a shadow mask. The distance between source and drain electrodes was approximately 200 μm . For the electrical measurements of the CNFs, approximately 60 devices for each of four different types of CNFs were fabricated and characterized.

2.5. Electrochemical characterization

The electrochemical measurements were performed using a symmetric two-electrode system that was constructed based on the electrode materials using four different types of CNF films ($1 \text{ cm} \times 1 \text{ cm}$) on the Ni foam; further, the electrode materials used for the electrical conductivity measurements were prepared under the same conditions as the CNF electrode films. The electrolyte used was an aqueous of 6 M KOH. Cyclic voltammetry (CV) measurements were carried out at a scan rate of 10 mV s^{-1} in a voltage range of 0.0–1.0 V using a potentiostat/galvanostat (Eco Chemie, PGST302N). The galvanostatic charge/discharge measurements were performed at a current density of $0.2\text{--}10 \text{ A g}^{-1}$ in a voltage range of 0.0–1.0 V using a battery cycler system (Won-A Tech., WMPG 3000). The electrochemical impedance spectroscopy (EIS) measurements were measured by fresh cells in a frequency range of 100 kHz to 10 mHz at an AC signal of 10 mV.

3. Results and discussion

Fig. 1 shows FESEM images of the CNFs, PCNFs, Pt/CNFs, and Pt/PCNFs. All samples display uniform morphologies and smooth surfaces. The diameters of the nanofibers were found to be 217–235 nm for the CNFs (Fig. 1a), 214–223 nm for the PCNFs (Fig. 1b), 222–249 nm for the Pt/CNFs (Fig. 1c), and 212–231 nm for the Pt/PCNFs (Fig. 1d). In particular, the Pt/CNFs and Pt/PCNFs

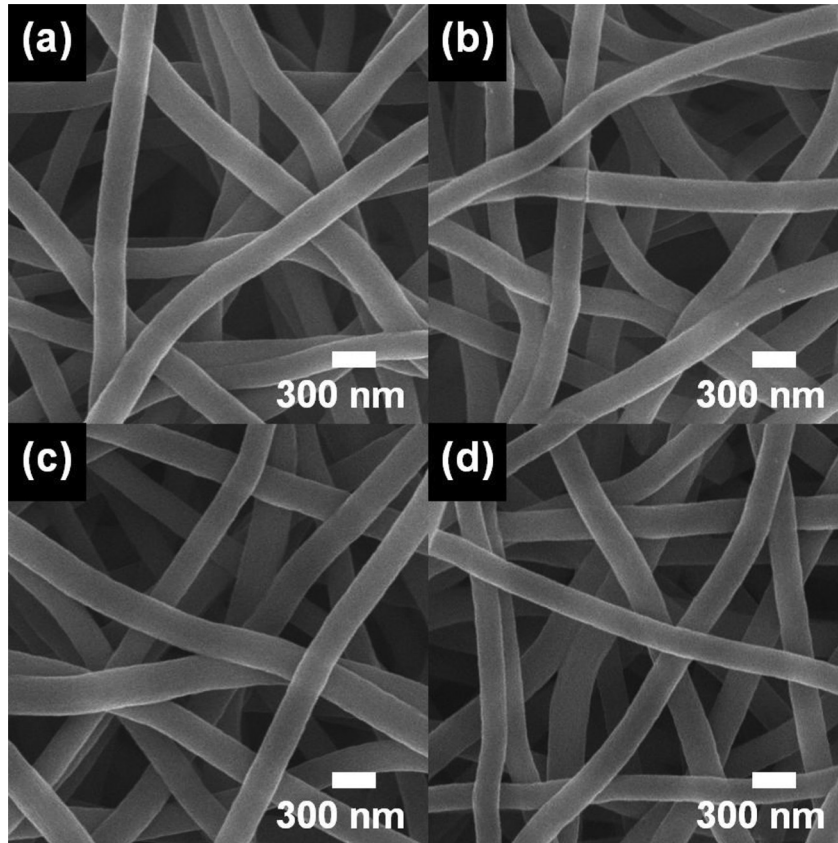


Fig. 1. FESEM images of the CNFs, PCNFs, Pt/CNFs, and Pt/PCNFs.

exhibited the formation of uniform nanofibers without any beads of agglomerated Pt on the surface, implying that the Pt nanoparticles were uniformly embedded within the CNFs.

The morphological and structural properties of the four different types of individual CNFs were further characterized using TEM, as shown in Fig. 2. The CNFs show uniform contrast along their bodies (Fig. 2a and e), whereas the PCNFs show non-uniform contrast along their bodies due to the existence of small pores within the CNFs (Fig. 2b and f). These small pores can be achieved

by the decomposition of SAN in as-spun nanofibers during the carbonization process [18]. In addition, an excellent distribution of Pt nanoparticles with a size range of 7–10 nm in the Pt/CNFs can be observed, as shown in Fig. 2c. Importantly, Pt/PCNFs show a unique structure with well-distributed pores and Pt nanoparticles of 7–10 nm-size in the Pt/PCNFs, as shown in Fig. 2d and h.

Fig. 3a shows XRD patterns obtained from the CNFs, PCNFs, Pt/CNFs, and Pt/PCNFs. All samples show a broad peak at approximately 25° , corresponding to the (002) layers of graphite. The main

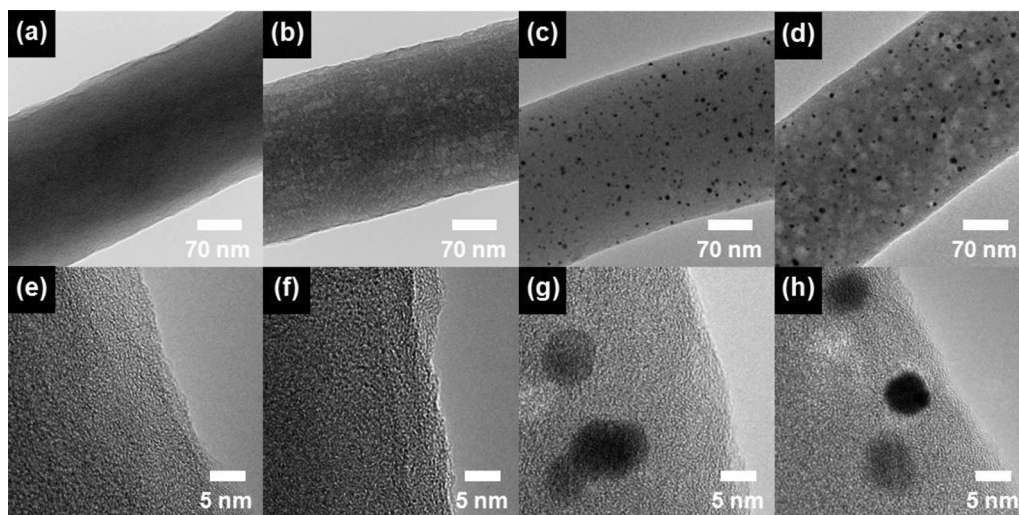


Fig. 2. TEM images (a–d) and HRTEM images (e–h) of the CNFs, PCNFs, Pt/CNFs, and Pt/PCNFs.

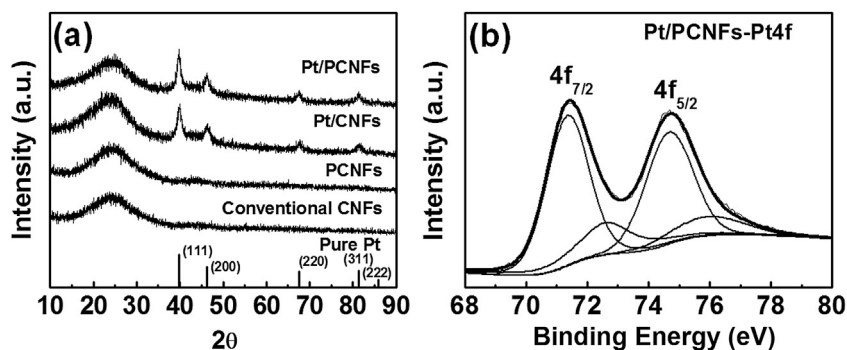


Fig. 3. (a) XRD patterns of the CNFs, PCNFs, Pt/CNFs, and Pt/PCNFs. (b) XPS core-level spectra of Pt $4f_{7/2}$ and Pt $4f_{5/2}$ of Pt/PCNFs.

diffraction patterns of the Pt/CNFs and Pt/PCNFs can be observed at $2\theta = 39.7^\circ$, 46.2° , 67.5° , and 81.3° , corresponding to the (111), (200), (220), and (311) crystal planes of metallic Pt with a face-centered cubic structure (space group $Fm\bar{3}m[225]$) (JCPDS card No. 04-0802). From the diffraction patterns of the Pt/CNFs and Pt/PCNFs, the grain sizes of the Pt nanoparticles can be calculated using the Scherrer equation, which is given below:

$$D = 0.9\lambda/(\beta \cos \theta) \quad (1)$$

where λ , β , and θ are the X-ray wavelength, the full width at half maximum (FWHM), and the Bragg angle. The average sizes of the Pt nanoparticles are estimated to be 8.7 nm for the Pt/CNFs and 8.8 nm for the Pt/PCNFs, based on the (111), (200), and (220) planes, which is consistent with the TEM results (Fig. 2d and h). This finding is also well supported by the corresponding XPS data, which are shown in Fig. 3b. To verify the existence of well-distributed Pt nanoparticles in the Pt/CNFs and Pt/PCNFs, XPS measurements were carried out. The XPS core-level spectra from Pt $4f_{7/2}$ and Pt $4f_{5/2}$ photoelectrons are observed at ~ 71.3 eV and ~ 74.6 eV, respectively, which correspond to the metallic Pt phases.

To investigate the porosity types (e.g. microporous and mesoporous) of the CNFs, PCNFs, Pt/CNFs, and Pt/PCNFs, N_2 adsorption/desorption isotherms were examined by BET measurements, as shown in Fig. 4. The isotherms for the PCNFs present type I characteristics, based on the international union of pure and applied chemistry (IUPAC), indicating the presence of microporous pores (pore width < 2 nm) at relative low pressures ($P/P_0 < 0.1$). In contrast, the isotherms for the Pt/PCNFs exhibit combined characteristics of types I/IV, indicating the presence of mesoporous pores

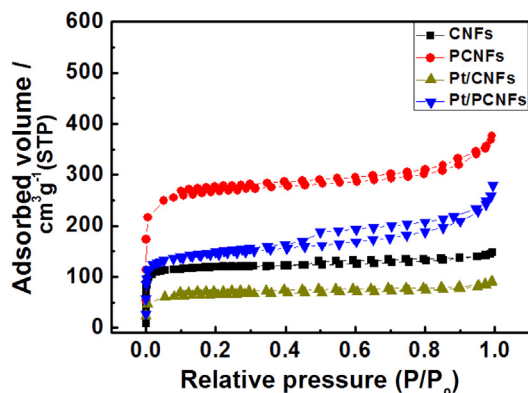


Fig. 4. N_2 adsorption/desorption isotherms of the CNFs, PCNFs, Pt/CNFs, and Pt/PCNFs.

(pore width 2–50 nm, IUPAC) classification at an intermediate relative pressure ($P/P_0 = 0.4$) [19]. Detailed information of specific surface areas, pore volumes, average pore diameters, and a pore volume fractions for the CNFs, PCNFs, Pt/CNFs, and Pt/PCNFs is summarized in Table 1. The specific surface area of the Pt/PCNFs is 1.5 and 2.7 times higher than that of the CNFs and Pt/CNFs, respectively. As summarized in Table 1, the specific surface area for the two types of porous CNFs (PCNFs and Pt/PCNFs) is increased compared to nonporous CNFs (CNFs and Pt/CNFs), and the mesopore volume fraction of the Pt/CNFs and Pt/PCNFs is significantly much higher than those of the CNFs and PCNFs without Pt nanoparticles. Additionally, the average size of the pores and the mesopore volume fraction increase with the addition of Pt nanoparticles, which can be attributed to an oxidation–reduction reaction between the oxidation sources in the Pt precursor ($H_2PtCl_6 \cdot xH_2O$) and the carbon during the CNF formation process [20,21].

Importantly, the nano-sized Pt-embedded PCNFs can exhibit characteristics of high surface area with a large mesopore volume as well as high electrical conductivity due to the distribution of the Pt metallic phase as a result of the electrospinning and carbonization processes, resulting in enhanced electrochemical performance. In addition, mesopores can provide a shorter diffusion route and low resistance pathways for the ions through the porous structure because large mesopores are more favorable for ion diffusion at high speeds and high current densities, based on the efficient utilization of specific surface areas [22]. Accordingly, we examined the electrical and electrochemical properties to investigate the relationship between the porous structure of carbon materials and the electrical conductivity due to Pt metallic-nanophase embedded PCNFs.

For measurements of the electrical conductivity for four different types of CNFs, we fabricated two-terminal CNF devices. A total of 237 devices were fabricated and characterized: 60 devices for CNFs, 59 devices for PCNFs, 59 devices for Pt/CNFs, and 59 devices for Pt/PCNFs. As shown in Fig. 5, CNFs and PCNFs without Pt metallic nanophases exhibited relatively higher electrical

Table 1

List of a specific surface area, a pore volume, an average pore diameter, and a pore volume fraction for CNFs, PCNFs, Pt/CNFs, and Pt/PCNFs.

Samples	S_{BET} [$m^2 g^{-1}$]	Total pore volume ($p/p_0 = 0.990$) [$cm^3 g^{-1}$]	Average pore diameter [nm]	Pore volume fraction	
				V_{micro} (%)	V_{meso} (%)
CNFs	443	0.22	2.3	84.3	15.7
PCNFs	1071	0.61	1.9	82.8	17.2
Pt/CNFs	245	0.13	2.8	46.4	53.6
Pt/PCNFs	670	0.30	2.9	44.3	55.7

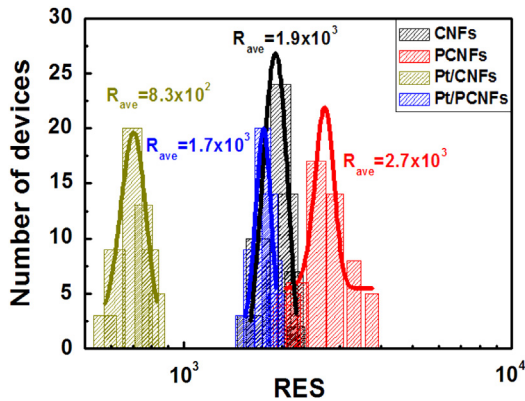


Fig. 5. Average electrical resistance of the CNFs, PCNFs, Pt/CNFs, and Pt/PCNFs.

resistance than Pt/CNFs and Pt/PCNFs, indicating that the increase in conductivity is due to well-distributed Pt nanoparticles in the CNFs. As shown in Fig. 5, average electrical resistance (R_{ave}) of CNFs, PCNFs, Pt/CNFs, and Pt/PCNFs were 1.9×10^3 , 2.7×10^3 , 8.3×10^2 , and 1.7×10^3 , respectively.

Next, to investigate the electrochemical properties of the prepared samples as electrochemical capacitor electrodes, we first examined cyclic voltammetry (CV) measurements at a scan rate of 10 mV s^{-1} in a voltage range of 0.0–1.0 V in 6 M KOH aqueous electrolyte, as shown in Fig. 6a. In general, the critical factors that strongly affect the electrochemical performance of EDLCs are the surface area of the carbon-based materials, pore size, presence of large mesopores (2–50 nm), and low resistivity in the containing carbon nanofibrous system [5,16,22]. In Fig. 6a, the Pt/PCNF electrode exhibited a significantly larger quasi-rectangular shape with the least slope at approximately 0.9–1 V, indicating the expansion of the electrical double-layer region due to a large surface area with a suitable mesopore volume fraction and good electrical conductivity [23]. The specific capacitance (C_{sp}) at the current density of

$0.2\text{--}10 \text{ A g}^{-1}$ of all electrodes (Fig. 6b) was calculated using the following equation [24,25]:

$$C_{sp} = 4I / (m dV / dt) \quad (2)$$

where I (A) is the discharge current, m (g) is the total mass of the active materials, dV is the voltage drop upon discharging, and dt (s) is the total discharge time. The specific capacitances were measured at the current density of 0.2 A g^{-1} for the CNF electrode, the PCNF electrode, the Pt/CNF electrode, and the Pt/PCNF electrode, yielding values of ~ 37.5 , 118.7, 50.0 and 130.2 F g^{-1} , respectively. In addition, the specific capacitance decreased slightly with an increase in the current density from 0.2 to 10 A g^{-1} in aqueous electrolytes, as shown in Fig. 6b. The Pt/PCNF electrode had a greater specific capacitance at all current densities, which can be attributed to the synergistic effects of a large specific surface area, the increased mesopore volume fraction, and the improved electrical conductivity as a result of the Pt metallic nanoparticles in this electrode. This conclusion is also well supported by TEM results (Fig. 2) and XRD results (Fig. 3). Surprisingly, the Pt/PCNFs electrode showed superior high-rate performance for a specific capacitance retention of 90% at a discharge current of 10 A g^{-1} .

In the Ragone plot (Fig. 6c), the energy density (E , Wh kg^{-1}) and power density (P , W kg^{-1}) were calculated using the following equation [26]:

$$E = C_{sp} V^2 / 8 \quad (3)$$

$$P = E / dt \quad (4)$$

where C is the specific capacitance of the two-electrode capacitor, V is the discharge voltage, and dt (s) is the total discharge time. In the case of the electrode materials (CNFs and PCNFs) without Pt nanoparticles, the energy density decreased rapidly with increasing power density. The Pt/PCNF electrode showed the highest energy density of $16.9\text{--}15.4 \text{ Wh kg}^{-1}$ in the power density range from 555 to $27,843 \text{ W kg}^{-1}$ than other electrodes. Furthermore, the Pt/PCNF

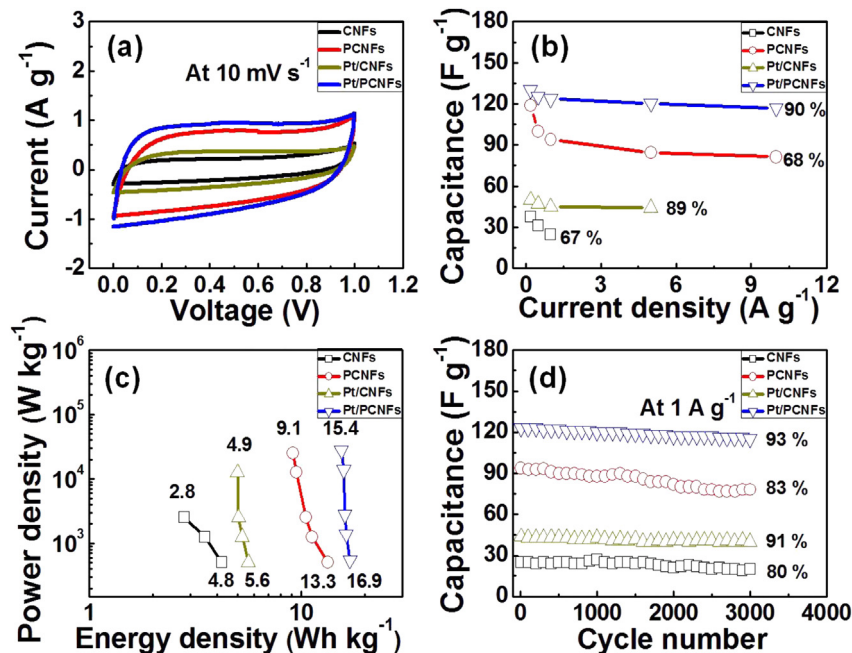


Fig. 6. (a) Cyclic voltammetry (CV) measurements at a scan rate of 10 mV s^{-1} in a voltage range of 0.0–1.0 V. (b) Specific capacitance at a current density of $0.2\text{--}10 \text{ A g}^{-1}$. (c) A Ragone plot for the CNF electrode, the PCNF electrode, the Pt/CNF electrode, and the Pt/PCNF electrode. (d) Cycling durability at a current density of 1 A g^{-1} up to 3000 cycles.

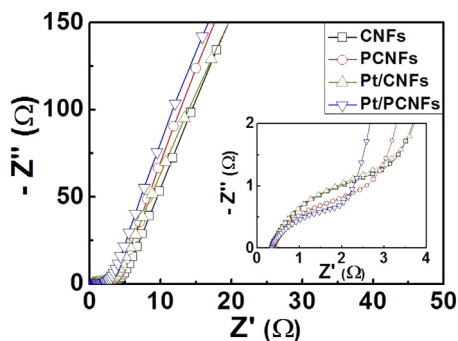


Fig. 7. Nyquist plots of all electrodes in the frequency range of 100 kHz to 10 mHz at an AC signal of 10 mV using fresh cells.

electrode exhibited good cycling stability with the specific capacitance retention of 93% at current density of 1 A g^{-1} up to 3000 cycles, as shown in Fig. 6d. Fig. 7 shows the Nyquist plots of the electrodes in a frequency range of 100 kHz to 10 mHz at an AC signal of 10 mV. In the high-frequency range, the Pt/PCNF electrode displays the smallest semicircular loop among other samples, implying that the lowest charge transfer resistance at the electrode/electrolyte interface. In the low-frequency range, a straight line of the Pt/PCNF electrode is more vertical along an imaginary axis compared to other samples, which means improved ion diffusion in solution and increased adsorption/desorption of ions onto the electrode surface.

Based on the electrochemical characterization results, the Pt/PCNFs achieved high-performance EDLC behaviors compared to other samples, when accounting for similar CNF diameters. This performance improvement can be explained by two major effects. First, a high surface area with a large mesopore volume was developed relative to the increased charge transport, which was more favorable for ion diffusion at high current densities due to the increased active areas and shorter diffusion routes. Second, the improved electrical conductivity was improved relative to the more efficient transport of electrons in the electrodes as a result of the low electrical resistance of the electrodes, which resulted in well-distributed Pt nanoparticles in the CNFs [27,28]. Further, we believe that the high surface areas with large mesopore volumes are very important factors for obtaining high-performance EDLCs with improved electrical conductivity. In other words, the Pt/PCNFs exhibited superior electrochemical performance due to the effect of synergy such as a high surface area with a large mesopore volume and their improved electrical conductivity.

4. Conclusions

Pt/PCNFs with a high specific surface area and well-developed mesopores have been successfully synthesized using an electrospinning method and their performance in an electrical double-layer capacitor (EDLC) has been characterized. The Pt/PCNFs exhibited the enhancement of a high specific surface area of

$670 \text{ m}^2 \text{ g}^{-1}$, a total pore volume of $0.30 \text{ cm}^3 \text{ g}^{-1}$, a large volume percentage of mesopores of 55.7%, and a low electrical resistance of 1.7×10^3 . Compared with the use of CNF, PCNF, and Pt/CNF electrode materials in EDLCs, the Pt/PCNF electrode led to the highest specific capacitance of 130.2 F g^{-1} at a current density of 0.2 A g^{-1} , high-rate performance with a specific capacitance retention of 90% in the range $0.2\text{--}10 \text{ A g}^{-1}$, superior cycling durability with a specific capacitance retention of 93% up to 3000 cycles, and a promising energy density of $16.9\text{--}15.4 \text{ W h kg}^{-1}$ in the power density range from 555 to $27,843 \text{ W kg}^{-1}$. Therefore, the electrochemical high-performance of Pt/PCNFs may be attributed to the synergic effects of high surface area with large mesopores volume and their improved electrical conductivity.

Acknowledgments

This research was supported by Basic Science Research Program through the National Research Foundation of Korea (NRF) funded by the Ministry of Education, Science and Technology (2012-007444).

References

- [1] P. Simon, Y. Gogotsi, B. Dunn, *Science* 343 (2014) 1210–1211.
- [2] P. Simon, Y. Gogotsi, *Nat. Mater.* 7 (2008) 845–854.
- [3] M. Inagaki, H. Konno, O. Tanaiki, *J. Power Sources* 195 (2010) 7880–7903.
- [4] J.H. Jang, S. Han, T. Hyeon, S.M. Oh, *J. Power Sources* 123 (2003) 79–85.
- [5] G.-H. An, H.-J. Ahn, *Carbon* 65 (2013) 87–96.
- [6] M. Zhi, C. Xiang, J. Li, M. Li, N. Wu, *Nanoscale* 5 (2013) 72–88.
- [7] G. Yu, X. Xie, L. Pan, Z. Bao, Y. Cui, *Nano Energy* 2 (2013) 213–234.
- [8] Y. Huang, J. Liang, Y. Chen, *Small* 8 (2012) 1805–1834.
- [9] X. Ma, L. Gan, M. Liu, P.K. Tripathi, Y. Zhao, Z. Xu, D. Zhu, L. Chen, *J. Mater. Chem. A* 2 (2014) 8407–8415.
- [10] Y. Guo, Z. Shi, M. Chen, C. Wang, *J. Power Sources* 252 (2014) 235–243.
- [11] D. Bhattacharjya, J.-S. Yu, *J. Power Sources* 262 (2014) 224–231.
- [12] J.P.C. Trigueiro, R.L. Lavall, G.G. Silva, *J. Power Sources* 256 (2014) 264–273.
- [13] G.-H. An, H.-J. Ahn, *Ceram. Int.* 38 (2012) 3197–3201.
- [14] G.-H. An, H.-J. Ahn, *Electrochem. Solid-State Lett.* 3 (2014) M29–M32.
- [15] G.-H. An, H.-J. Ahn, *J. Electroanal. Chem.* 707 (2013) 74–77.
- [16] B.-H. Kim, K.S. Yang, Y.A. Kim, Y.J. Kim, B. An, K. Oshida, *J. Power Sources* 196 (2011) 10496–10501.
- [17] L.-F. Chen, X.-D. Zhang, H.-W. Liang, M. Kong, Q.-F. Guan, P. Chen, Z.-Y. Wu, S.-H. Yu, *ACS Nano* 8 (2012) 7092–7102.
- [18] B.-S. Lee, S.-B. Son, K.-M. Park, W.-R.I. Yu, K.-H. Oh, S.-H. Lee, *J. Power Sources* 199 (2012) 53–60.
- [19] W. Li, F. Zhang, Y. Dou, Z. Wu, H. Liu, X. Qian, D. Gu, Y. Xia, B. Tu, D. Zhao, *Adv. Energy Mater.* 1 (2011) 382–386.
- [20] G.-H. An, S.-J. Kim, K.-W. Park, H.-J. Ahn, *Electrochem. Solid-State Lett.* 3 (2014) M21–M23.
- [21] Z. Yang, G. Du, Z. Guo, X. Yu, S. Li, Z. Chen, P. Zhang, H. Liua, *Nanoscale* 2 (2010) 1011–1017.
- [22] Q. Li, R. Jiang, Y. Dou, Z. Wu, T. Huang, D. Feng, J. Yang, A. Yu, D. Zhao, *Carbon* 49 (2011) 1248–1257.
- [23] B.-H. Kim, K.S. Yang, H.-G. Woo, K. Oshida, *Synth. Met.* 161 (2011) 1211–1216.
- [24] M. Liu, W.W. Tjiu, J. Pan, C. Zhang, W. Gao, T. Liu, *Nanoscale* 6 (2014) 4233–4242.
- [25] X. Li, W. Xing, S. Zhuo, J. Zhou, F. Li, S.-Z. Qiao, G.-Q. Lu, *Bioresour. Technol.* 102 (2011) 1118–1123.
- [26] X. Yang, L. Zhang, F. Zhang, T. Zhang, Y. Huang, Y. Chen, *Carbon* 72 (2014) 381–386.
- [27] B.-H. Kim, K.S. Yang, J.P. Ferraris, *Electrochim. Acta* 75 (2012) 325–331.
- [28] G.-H. An, H.-J. Ahn, *Electrochem. Solid-State Lett.* 2 (2013) M33–M36.